PAPER

The stability of LaMnO₃ surfaces: a hybrid exchange density functional theory study of an alkaline fuel cell catalyst

E. A. Ahmad,*[ab] G. Mallia,[ab] D. Kramer,[ac] A. R. Kucernak[a] and N. M. Harrison[abd]

LaMnO₃ is an inexpensive alternative to precious metals (*e.g.* platinum) as a catalyst for the oxygen reduction reaction in alkaline fuel cells. In fact, recent studies have shown that among a range of non-noble metal catalysts, LaMnO₃ provides the highest catalytic activity. Despite this, very little is known about LaMnO₃ in the alkaline fuel cells environment, where the orthorhombic structure is most stable. In order to understand the reactivity of orthorhombic LaMnO₃ we must first understand the surface structure. Hence, we have carried out calculations on its electrostatically stable low index surfaces using hybrid-exchange density functional theory, as implemented in CRYSTAL09. For each surface studied the calculated structure and formation energy is discussed. Among the surfaces studied the (100) surface was found to be the most stable with a formation energy of 0.98 J m⁻². The surface energies are rationalised in terms of the cleavage of Jahn–Teller distorted Mn–O bonds, the compensation of undercoordination for ions in the terminating layer and relaxation effects. Finally, the equilibrium morphology of orthorhombic LaMnO₃ crystals is predicted, allowing us to speculate about likely surface reaction sites.

I Introduction

LaMnO₃ belongs to a class of ABO₃ perovskites, which are well known for their magnetic properties and applications in solid oxide fuel cells (SOFCs).[1–3] These materials are also used in magnetic refrigeration,[4] metal-air batteries[5] and alkaline fuel cells (AFCs).[6] Although the use of perovskites-type oxides as oxygen reduction reaction (ORR) catalysts was first explored in 1970,[7] until the last decade, this class of material had not been studied for alkaline fuel cell (AFC) applications. In 2004, LaMnO₃ was identified as a viable ORR catalyst for alkaline fuel cells (AFCs),[6] with activity comparable to Pt. A review of alkaline fuel cell cathodes[8] has subsequently shown that the performance of LaMnO₃ is among the highest of non-noble metal catalysts. Furthermore, a systematic study of the variation in catalytic activity with the d-electron occupancy of various perovskite oxides has shown that LaMnO₃ has optimal catalytic activity for the ORR reaction.[9] It is claimed that this is because LaMnO₃ possesses an ideal d-electron occupancy (d⁴), with neither too weak nor too strong O₂ interactions.[9]

There have been extensive theoretical and experimental studies of the structure and properties of bulk LaMnO₃ (see our

[a]Department of Chemistry, Imperial College London, South Kensington, London SW7 2AZ, UK. E-mail: ehsan.ahmad08@imperial.ac.uk

[b]Thomas Young Centre, Imperial College London, South Kensington, London SW7 2AZ, UK

[c]Faculty of Engineering and the Environment, University of Southampton, University Road, Southampton SO17 1BJ, UK

[d]STFC, Daresbury Laboratory, Daresbury, Warrington, WA4 4AD, UK

previous work[10] and the references therein). At low temperature, the structure is orthorhombic with an A-type antiferromagnetic (AAF) insulating ground state.[11] This is due to a Jahn–Teller (J–T) distortion that breaks the degeneracy of the Mn³⁺ 3d⁴ orbitals. At high temperature (750 K) the geometry adopts cubic symmetry as the thermal vibrations lift the J–T distortion.[12] In contrast with the bulk, relatively little is known about the surface structures and properties of LaMnO₃. To the best of our knowledge, there have been no experimental studies on the structure and properties of the surfaces and terminations of LaMnO₃, in either the high temperature cubic phase or the low temperature orthorhombic phase. However, various theoretical works, based on density functional theory (DFT), have been carried out to calculate the formation energies and structures of the surfaces.[13–15] The consensus from these studies is that the MnO₂ terminated (001) surface is the most stable in both phases (in the orthorhombic case this corresponds to the surface perpendicular to longest lattice parameter, *i.e.* in the *Pnma* setting this is the (010) surface). These calculations also predict that the surface is sensitive to environmental conditions[15] and adsorbed species,[16] which can lead to alternate low energy surfaces.

The adsorption of oxygen on the surface of LaMnO₃ has been simulated,[16–18] focusing mainly on the high temperature (cubic) surface for SOFC applications. These studies conclude that oxygen is most likely to adsorb on the Mn sites, and that dissociative adsorption is more favourable than molecular adsorption; this is contrary to what is observed on the isomorphic material SrTiO₃, where calculations show that the adsorbing O atoms prefer the bridge position between Ti and O ions.[16] A

mechanism has also been proposed for the adsorption, dissociation and diffusion of O on $LaMnO_3$ surfaces, in which the adsorbed O passes through superoxide (O_2^-) and peroxide (O_2^{2-}) states before dissociating into O ions that are incorporated into the lattice.[17] Finally, the adsorption of various ORR intermediates on the (001) surfaces of $LaMnO_3$, $LaCrO_3$ and $LaFeO_3$ has indicated that $LaMnO_3$ is optimal for ORR activity.[19] This is based on the binding strength of the intermediates, calculated using hybrid methods, being neither too strong nor too weak compared to the other materials.

Previous theoretical work on the structure of the $LaMnO_3$ surface has mainly concentrated on its application in SOFCs, which is not directly applicable to AFCs as the ORR follows different pathways in the different fuel cell types. O_2 is reduced to O^{2-} ions that diffuse into a solid electrolyte in the SOFC, while in the AFC O_2 reacts with H_2O to form OH^- ions that pass into a liquid electrolyte. Furthermore, the AFC operating temperature is significantly lower than that of SOFCs, meaning that $LaMnO_3$ is stable in the orthorhombic rather than cubic phase. Theoretical studies relevant to low temperature systems must, therefore, consider the more complex orthorhombic system. The bulk crystal of the orthorhombic phase of $LaMnO_3$ consists of an ordered array of J–T distorted MnO_6 octahedra. Studies of the surface atomic structure must therefore take into account the effects of local J–T distortions of the octahedra and their ordering in the near surface region.[10,20,21] Tang *et al.* have reported DFT calculations that show the effects of J–T distortion on the surface of orthorhombic $LaMnO_3$,[22] where they reported the % displacement of the surface atoms upon relaxation with respect to the unrelaxed geometry cut from the optimized bulk. However, their study was limited to the (001) surface only. No comprehensive study of the range of surfaces and terminations that are possible with orthorhombic $LaMnO_3$ has been published.

In this study, the structure and energetics of the orthorhombic (*Pnma*) $LaMnO_3$ surfaces are investigated systematically by constructing and relaxing all of the possible low index surfaces – (*hkl*), with $|h|$, $|k|$ and $|l| \leq 1$ – using hybrid-exchange DFT with the Becke, three-parameter Lee–Yang–Parr (B3LYP) functional (as implemented in CRYSTAL09 (ref. 23 and 24)). The factors affecting the stability of the surfaces (J–T distortion, transition metal ion coordination at the surface and relaxation effects) are also studied in detail. The B3LYP functional is adopted for this study, as it provides an accurate description of the electronic structure of systems in which strong electron–electron interactions result in electron localisation and orbital ordering (particularly for transition metal oxides),[20,25–34] and has recently been shown to provide quantitative agreement between calculated and experimental formation energies for the Mn-oxides.[10]

This paper is organised as follows. The methodology is provided in Section II and III contains the computational details. The results are presented in Section IV. Here the structure of the studied surfaces before and after relaxation is discussed, followed by a detailed analysis into the effects of J–T distortion, bond cleavage, the compensation of ion undercoordination and relaxation effects on the surface formation energies. Electron density difference maps are used to highlight the polarisation of the undercoordinated ions and a Wulff construction is used to analyse the %

coverage of the surfaces in the equilibrium crystal morphology. Finally Section V summarises the main findings of this study.

II Methodology

The surfaces of orthorhombic $LaMnO_3$ have been studied by adopting a slab model, which is periodic in two directions and consists of a sequence of atomic layers – parallel to the planes defined by the Miller indices (*hkl*) – cut from the optimized bulk geometry that has been reported previously.[10] In order to assess the stability of the various surfaces, the surface formation energy per unit area, E_s, is:

$$E_s = \frac{1}{2A}\left(E_{slab} - nE_{bulk}\right) \qquad (1)$$

where E_{slab} is the total energy of the slab per unit cell of area A containing n formula units, and E_{bulk} is the total energy per formula unit in the bulk. Eqn (1) does not take into account the influence of the chemical environment, and is only applicable to slabs with bulk stoichiometry.

All of the low index surfaces of the orthorhombic (*Pnma*) $LaMnO_3$ phase, as determined by cleaving the relaxed bulk structure,[10] are listed in Table 1. These surfaces can be analysed and classified according to the charge q (assuming formal charges for all ions) of each atomic layer and the dipole moment perpendicular to the surface μ_z of a stoichiometric repeat unit of atomic layers.[35] Upon examining the atomic layers of the planes in Table 1, it is evident that orthorhombic (*Pnma*) $LaMnO_3$ cannot form any low index Tasker Type 1 surfaces, since there are no neutral atomic layers ($q \neq 0$).[35] However, it is possible to take the charged atomic layers and construct symmetric slabs so that there is no dipole moment perpendicular to the surface ($\mu_z = 0$), corresponding to Tasker Type 2 surfaces. This is achieved by choosing the appropriate terminating atomic layer, restricting us to the options listed in Table 2 for unreconstructed surfaces.

The (010), (011) and (111) surfaces are Tasker Type 3 and cannot form Tasker Type 2 by choosing a suitable terminating layer. This type of surface is characterised by a dipole moment ($\mu_z \neq 0$) and results in a surface energy that is infinite, based on purely electrostatic considerations.[35] Reconstructions, chemical adsorptions and charge transfer can quench the macroscopic dipole and stabilise a Tasker Type 3 surface. The focus of this study, however, is on the surface energetics and relaxation of the orthorhombic phase of $LaMnO_3$, the features of which can be more easily isolated on the less complex unreconstructed stoichiometric surfaces listed in Table 2.

III Computational details

All calculations have been performed using the CRYSTAL09 (ref. 24) code, based on the expansion of the crystalline orbitals as a linear combination of a local basis set (BS) consisting of atom centred Gaussian orbitals. The Mn and O ions are described by a triple valence all-electron BS: an 86-411d(41) contraction (one s, four sp, and two d shells) and an 8-411d(1) contraction (one s, three sp, and one d shells), respectively; the most diffuse sp(d) exponents are $\alpha^{Mn} = 0.4986(0.249)$ and $\alpha^O = 0.1843(0.6$

Table 1 The atomic layer sequences of the low index surfaces of orthorhombic (*Pnma*) AAF LaMnO$_3$. In the column "Sequence", the stacking sequence of the atomic layers in the non-periodic direction (*z*) is indicated for the repeat unit of the slab; as regards notation, 2O–2La 2O–2O–2Mn, for instance, corresponds to a sequence of four layers as separated by hyphens. *n*-layers and *n*-atoms give the number of layers and of atoms in the repeat unit

Miller indices	Sequence	*n*-Layers	*n*-Atoms	Area (Å^2)	*a* (Å)	*b* (Å)
(1 0 0)	O–La–2O–2O–La–O–2Mn	7	10	43.425	5.614	7.735
(0 1 0)	2O–2La 2O–2O–2Mn	4	10	33.740	5.614	6.010
(0 0 1)	La–O–2O–2O–O–La–2Mn	7	10	46.483	6.010	7.735
(1 1 0)	O–La–O–O–O–O–La–O–2Mn	9	10	54.992	5.614	9.795
(1 0 1)	2O–La–La–O–2O–O–4Mn–O–2O–O–La–La–2O	13	20	63.611	7.735	8.224
(0 1 1)	2O–2O–2La–2O–2Mn–2O–2La–2O–2O–2Mn	10	20	57.437	6.010	9.558
(1 1 1)	O–O–O–La–La–O–O–O–2Mn	9	10	72.005	8.224	9.558

Table 2 The sequence of atomic layers of the low index surfaces of the orthorhombic (*Pnma*) LaMnO$_3$ phase simulated as Tasker Type 2 slabs in this work. The notation is as in Table 1

Miller indices	Sequence	*n*-Layers	*n*-Atoms	Thickness (Å)
(1 0 0)	2O–La–O–2Mn–O–La–2O	7	10	2.893
(0 0 1)	2O–O–La–2Mn–La–O–2O	7	10	2.523
(1 1 0)	O–O–La–O–2Mn–O–La–O–O	9	10	2.197
(1 0 1)	2O–La–La–O–2O–O–4Mn–O–2O–O–La–La–2O	13	20	3.753

Bohr^{-2}.[36] The La basis set includes a pseudopotential to describe the core electrons, while the valence part consists of a 411p(411)d(311) contraction scheme (with three s, three p and three d shells); the most diffuse exponent is $\alpha^{La} = 0.15$ Bohr^{-2} for each s,p and d.[20]

Electron exchange and correlation are approximated using the B3LYP hybrid-exchange functional, which, as noted above, is expected to be more reliable than the local density approximation (LDA) or generalised gradient approximation (GGA) approaches in this system.[25,28,37] The exchange and correlation potentials and energy functional are integrated numerically on an atom centred grid of points. The integration over radial and angular coordinates is performed using Gauss–Legendre and Lebedev schemes, respectively. A pruned grid consisting of 99 radial points and 5 sub-intervals with (146, 302, 590, 1454, 590) angular points has been used for all calculations (see the XXLGRID option in CRYSTAL09 (ref. 24)). This grid converges the integrated charge density to an accuracy of about $\times 10^{-6}$ electrons per unit cell. The Coulomb and exchange series are summed directly and truncated using overlap criteria with thresholds of 10^{-7}, 10^{-7}, 10^{-7}, 10^{-7} and 10^{-14} as described previously.[24,38] Reciprocal space sampling was performed on a Pack–Monkhorst net with a shrinking factor of IS = 8 (corresponding to an 8 × 8 × 8 grid in the reciprocal cell for the bulk and an 8 × 8 grid for the slabs). The self consistent field procedure was converged up to a tolerance in the total energy of $\Delta E = 1 \times 10^{-7}$ E_h per unit cell.

The internal coordinates of the slab have been determined by minimisation of the total energy within an iterative procedure based on the total energy gradient calculated analytically with respect to the nuclear coordinates. Convergence was determined from the root-mean-square (rms) and the absolute value of the largest component of the forces. The thresholds for the maximum and the rms forces (the maximum and the rms atomic displacements) have been set to 0.00045 and 0.00030 (0.00180 and 0.0012) in atomic units. Geometry optimisation was halted when all four conditions were satisfied simultaneously.

IV   Results and discussion

The Type 2 surfaces listed in Table 2 and the surface formation energies E_s are analysed in terms of bond cleavage, local geometry, relaxation and octahedral distortions. The different contributions to E_s can be disentangled by comparing the unrelaxed and relaxed slabs and defining the relaxation energy $E^{Relaxation}$ as the energy difference between them, which is normalised with respect to the surface area. The energy of the unrelaxed slab is used to rationalise the cost of cleavage by focusing on cleaved bonds and the truncation of octahedra at the surface terminations (note that by "bond" we do not imply a covalent bond but an Mn–O contact). For the relaxed slab we can focus on the specific local relaxations that increase $E^{Relaxation}$ and thus contribute to the stability of the surface.

In Fig. 1 the unrelaxed and relaxed E_s are presented as a function of slab thickness. The E_s value, converged with respect to the slab thickness for each surface, is also given in Table 3, where the surfaces are listed in the order of E_s. Both the unrelaxed and relaxed surfaces show the same order of stability, although the (001) and (101) surfaces become very similar in energy upon relaxation, due to the large relaxation of the (001) surface. The terminating oxygen layer of the (001) surface is also characterised by the greatest inward relaxation Δz of all the surfaces studied.

The average coordination of Mn at the termination of each surface is also included in Table 3. Surface cleavage reduces the
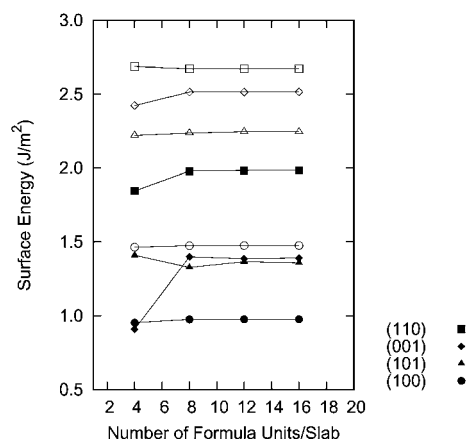
Fig. 1 The unrelaxed and relaxed surface formation energies E_s with increasing slab thickness, indicated as a function of the number of formula units of LaMnO$_3$ per slab. The unrelaxed and relaxed energies are indicated by the empty and filled points, respectively.

Table 3 The surface formation energies E_s of the stoichiometric Type 2 surfaces of orthorhombic (*Pnma*) AAF LaMnO$_3$. Mn^{coord} is the average coordination of the Mn in the surface layer. The inward/outward relaxation of the terminating oxygen is reported with a negative/positive Δz. $E_s^{Unrelaxed}$ and $E_s^{Relaxed}$ are the surface formation energies for the unrelaxed and relaxed surfaces, respectively; $E^{Relaxation}$ is the difference in energy between them, *i.e.* the surface area normalised energy of relaxation

Miller indices	Mn^{coord}	Δz (Å)	$E^{Relaxation}$ (J m^{-2})	$E_s^{Unrelaxed}$ (J m^{-2})	$E_s^{Relaxed}$ (J m^{-2})
(1 1 0)	4.5	0.028	*0.69*	2.67	1.98
(0 0 1)	5	−0.376	*1.13*	2.52	1.39
(1 0 1)	5.5	−0.038	*0.89*	2.25	1.36
(1 0 0)	5	−0.200	*0.49*	1.47	0.98

Mn coordination from the bulk value of 6. It has been argued that transition metal coordination to oxygen is the dominant factor in determining E_s and that E_s scales linearly with the loss of coordination.[39,40] However, for the surfaces we have studied, it is clear that the scaling of E_s is not linear with the Mn coordination, and that the (100) and (001) surfaces have a large difference in formation energy despite having the same Mn coordination. This behaviour is analysed further in Sections IV B and IV C.

The unrelaxed and relaxed structure of each surface are shown in Fig. 2–5 and discussed in detail in the following sections. The discussion is based on the comparison with the bulk geometry, which can be considered as a packing of corner-sharing MnO$_6$ octahedra with interstitial La ions. The octahedra are distorted due to the J–T effect, which breaks the degeneracy of the e$_g$ states of Mn^{3+}. Specifically, in each octahedron the Mn–O bond is elongated along a local apical axis (2.31 Å) and contracted in the equatorial planes (1.99 Å and 1.92 Å).[10] The interaction of these local distortions produces the orbital ordering observed in the bulk structure, which is correctly reproduced in our calculations.[10,21]

The relaxed octahedra at each surface are displayed in Fig. 2–5. On careful examination, it is evident that with respect to the bulk geometry there are significant surface relaxations,

which further distort the octahedra *via* additional rotation and tilt, and further shortening and lengthening of the Mn–O bonds. These effects also propagate through the sub-surface layers by means of the corner-sharing octahedra: geometrical changes which affect O ions linking octahedra lead to distortions that spread from the surfaces into the substrate.

Before we proceed to analyse each surface in more detail (from the highest to lowest E_s), it is important to note that a comparison with previous literature is not straightforward, since the Miller indices referring to a particular surface depend on the space group setting. For orthorhombic LaMnO$_3$, the standard space group setting is *Pnma* (no. 62), but in some of the previous works the *Pbnm* setting has been adopted;[13,15] in this case the set of lattice vectors **abc** of the *Pnma* setting are transformed into **cab**, *i.e.* the (110) surface of the *Pnma* setting adopted here corresponds to (011) of the *Pbnm* setting.[41,42]

A   structure and energetics

1   The (110) surface. The (110) surface layer is characterized by 4- and 5-coordinated Mn ions and an La ion, as can be seen from Fig. 2. When this surface is relaxed, the truncated octahedron centred at the 4-coordinated Mn is heavily distorted relative to the bulk, while the octahedron centred at the 5-coordinated Mn does not change significantly. There is also a slight outward movement of the La ions. In Fig. 2–5 the octahedron in the relaxed slab are only depicted as complete if the Mn–O bond distances are equal or less than the largest bulk Mn–O distance (2.31 Å for the apical bond). The incomplete octahedra in the sub-surface layers of the relaxed slab, therefore, indicate cases where the Mn–O distances have significantly increased. The elongated

Unrelaxed   Relaxed
E_s = 2.67 J/m^2 E_s = 1.98 J/m^2
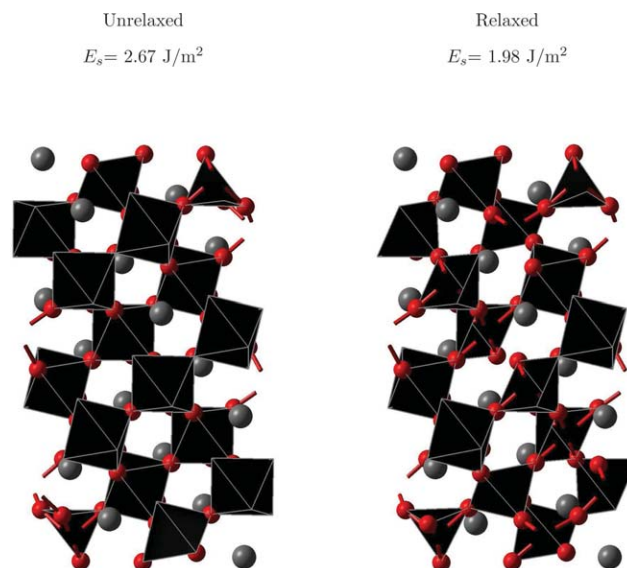
Fig. 2 The unrelaxed and relaxed slabs of the (110) surface are displayed and the corresponding formation energy reported. Large and small spheres correspond to the La and O ions, respectively. The Mn–O$_n$ unit is represented by a black polyhedron. Incomplete octahedra at the unrelaxed slab terminations indicate cleavage of Mn–O bonds. After relaxation, incomplete octahedra may also indicate a strong distortion by means of Mn–O bond elongation significantly beyond the largest bulk bond distance (the apical bond – 2.31 Å).

Mn–O bonds are 2.40 and 2.51 Å for the incomplete octahedra in the sub-surface layer nearest to the termination. The subsequent octahedra have elongated bonds that are 2.32 and 2.37 Å and only return to the bulk value of 2.31 Å 32 atomic layers (8.19 Å) below the surface. The relaxation of the terminating oxygen layer documented in Table 3 indicates an unusual expansion of the (110) surface. If we consider the atomic coordinates of the terminating atoms, it is evident that this surface exhibits a weak rumpling, where the outermost oxygen ion moves inward (by −0.02 Å) and the subsequent oxygen ion moves outward (by 0.07 Å) becoming the terminating ion. Overall the relaxation reduces the formation energy by 0.69 J m^{-2}.

The (110) surface of the orthorhombic phase has been previously studied by using an empirical electrostatic shell-model potential.[43] In this study, several terminating layers were studied and it was concluded that the Mn termination was the most stable. However, it is also reported that upon relaxation the La ions are promoted to the surface layer and thus the relaxed structure, which is otherwise dominated by Mn and O ions, will also contain La ions. This description of the relaxed surface is mostly in agreement with our findings.

2 The (001) surface. The (001) surface layer is terminated by O ions, which belong to truncated octahedra centered at 5-coordinated Mn ions. From Fig. 3, it can be seen that the truncated octahedra are tilted relative to the surface normal, and that the interstitial La ions are also exposed. Upon relaxation, the cleaved octahedra at the surface tilt and adopt a different orientation to the bulk. In order to allow this, the Mn–O bonds of the corner sharing octahedra in the sub-surface layers distort relative to the bulk. This occurs most notably in the third layer of Mn octahedra for the elongated apical Mn–O bond, which undergoes an increase from 2.31 Å to 2.33 Å, as indicated by the truncated octahedra in the relaxed slab of Fig. 3. These relaxation effects result in the largest inward displacement of the

terminating oxygen layer (0.376 Å) among all of the surfaces studied (see Table 3), as well as the largest $E^{Relaxation}$. Interestingly, the relaxation mostly affects the coordination and orientation of the Mn octahedra, while the La ions do not move significantly nor have any noticeable effect on their neighbouring O ions.

To the best of our knowledge, there are no previously published studies of the (001) surface of orthorhombic (Pnma) LaMnO₃.

3 The (101) surface. The (101) surface layer has fewer incomplete octahedra per unit cell than either the (110) or (001) surfaces, and this is reflected in its lower $E_s^{Unrelaxed}$, since fewer bonds have been cleaved. As evident in Fig. 4, only half of the terminating octahedra are incomplete, each exposing a 5-coordinated Mn. A unique feature of this surface is that the incomplete surface octahedron exposes the 5-coordinated Mn in a trough between two La ions. The remaining features of the surface are otherwise similar to the other surfaces considered, being terminated by O and exposing La ions.
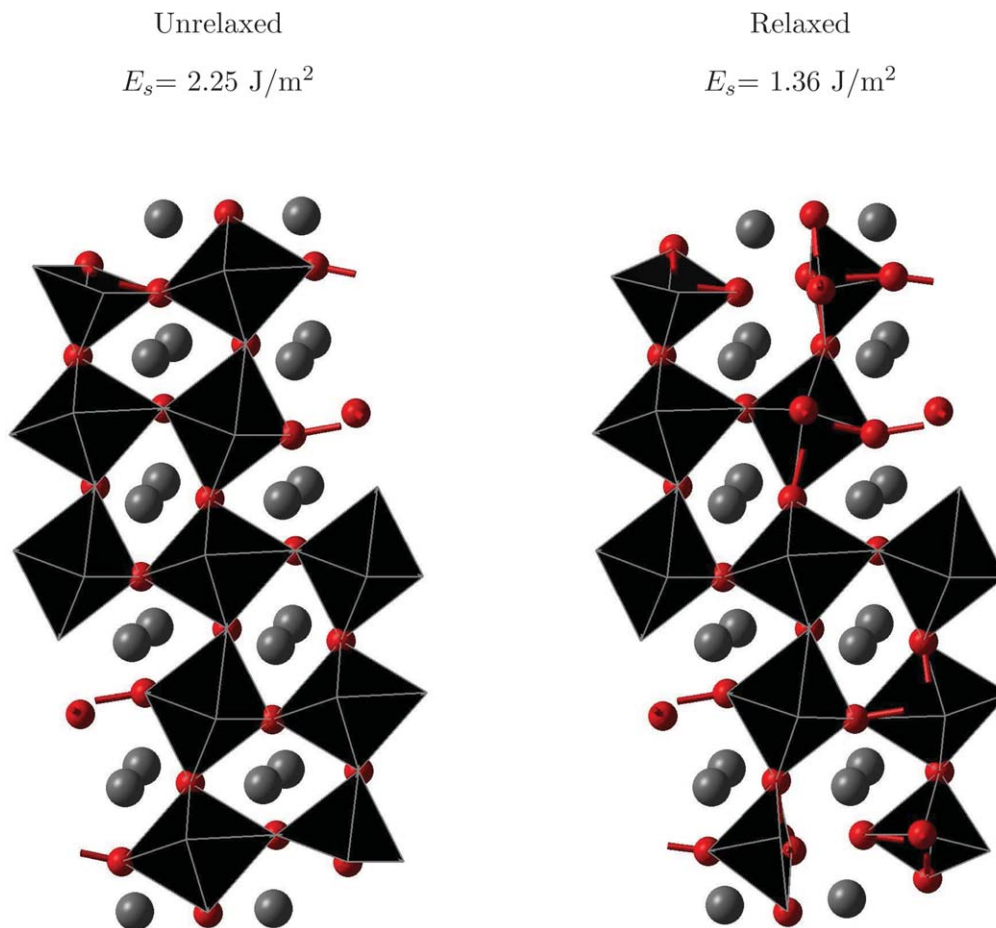
Upon relaxation of the (101) surface, the only significant change occurs on the terminal layer, where an apical Mn–O bond belonging to the terminating 6-coordinated octahedron is lengthened to 2.42 Å (as indicated by the newly truncated octahedron in the relaxed slab of Fig. 4). Since this relaxation occurs perpendicular to the surface normal, it is expected that the relaxation (in z) of the terminating oxygen layer would not be large (−0.038 Å, as reported in Table 3). The relaxation energy is, however, relatively high at 0.89 J m^{-2}, implying that the relaxation of the terminating oxygen layer is not necessarily an indicator of the relaxation energy of a surface.

The (101) surface of orthorhombic (Pnma) LaMnO₃ is equivalent to the (110) surface in the Pbnm setting. Using this alternative setting, previous studies have been published using a variety of approximations (unrestricted Hartree-Fock (UHF) linear combination of atomic orbitals (LCAO),[13] hybrid B3PW LCAO, generalised gradient approximation-plane wave (GGA-PW),[44] and GGA-PW91 (ref. 15)). Comparison of the data computed here is not possible as there is an apparent discrepancy in the description of the surface: the (110) atomic layer sequences in the previous studies do not correspond to the orthorhombic phase of LaMnO₃. The Pbnm (110) surface is reported with an atomic layer sequence of LaMnO–2O–LaMnO–2O, whereas the correct sequence (for Pnma (101)) is 2O–La–La–O–2O–O–4Mn–O–2O–O–La–La–2O (as reported in Table 2). The sequence in the previous studies appears to instead belong to the (110) surface of the cubic phase.
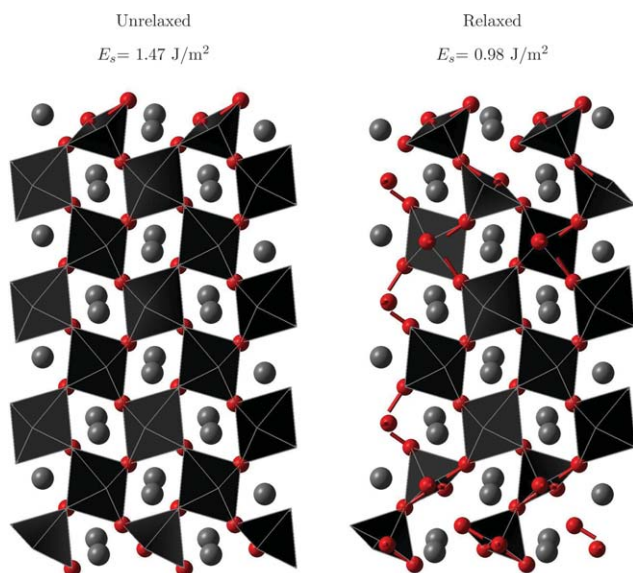
4 The (100) surface. The (100) surface is similar to the (001) surface (compare Fig. 3 and 5); the terminating layers of both contain 5-coordinated Mn, and the corresponding truncated octahedra share a similar orientation relative to the surface normal. Nevertheless $E_s^{Unrelaxed}$, of the (100) surface is much lower than that calculated for the (001) surface, and also significantly lower than the (101) surface, which actually has less Mn under-coordination. This result disagrees with the previously proposed model, which rationalises that the surface formation energies of oxides are dominated by the degree of metal coordination loss.[39,40] The energetics of the LaMnO₃ surfaces are

Unrelaxed
$E_s = 2.52$ J/m²
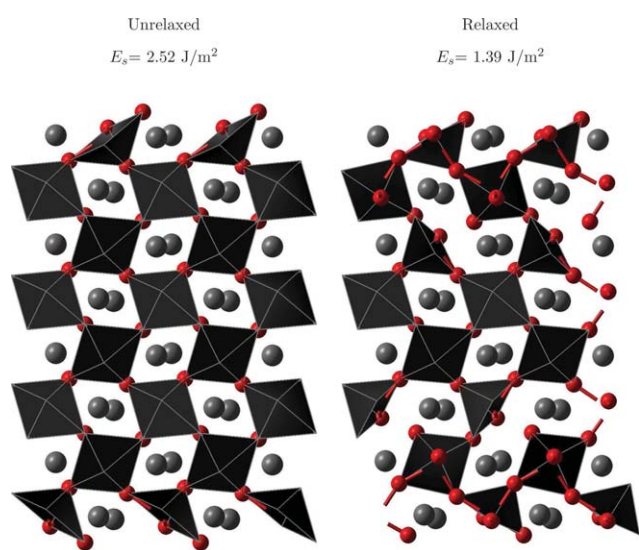
Relaxed
$E_s = 1.39$ J/m²

Fig. 3 The unrelaxed and relaxed slabs of the (001) surface. The unit cell of this surface has been repeated laterally for a clearer depiction of the octahedra. It is terminated by two Mn ions, one of which is symmetric to and hidden from view by the visible one. Remaining details are as in Fig. 2.

11156 | J. Mater. Chem. A, 2013, **1**, 11152–11162

This journal is © The Royal Society of Chemistry 2013

Unrelaxed

$E_s = 2.25 \ \mathrm{J/m^2}$

Relaxed

$E_s = 1.36 \ \mathrm{J/m^2}$

Fig. 4 The unrelaxed and relaxed slabs of the (101) surface. This surface is terminated by four Mn ions, two of which are symmetric to and obstructed from view by the visible two. Remaining details are as in Fig. 2.

Unrelaxed

$E_s = 1.47 \ \mathrm{J/m^2}$

Relaxed

$E_s = 0.98 \ \mathrm{J/m^2}$

Fig. 5 The unrelaxed and relaxed slabs of the (100) surface. The unit cell of this surface has been repeated laterally for a clearer depiction of the octahedra. It is normally terminated by two Mn ions, one of which is symmetric to and hidden from view by the visible one. Remaining details are as in Fig. 2.

governed by more complex phenomena than simple bond cleavage, as discussed in detail in the following section.

Upon relaxation, the terminating Mn octahedra do not tilt to the same degree observed on the (001) surface, but a set of apical Mn–O bonds in sub-surface layer are lengthened. This leads to an energy of relaxation and inward displacement roughly half of that for the (001) surface (see Table 3). As with the (001) surface, to the best of the authors knowledge there are no previous studies of the (100) surface of orthorhombic *Pnma* LaMnO$_3$.

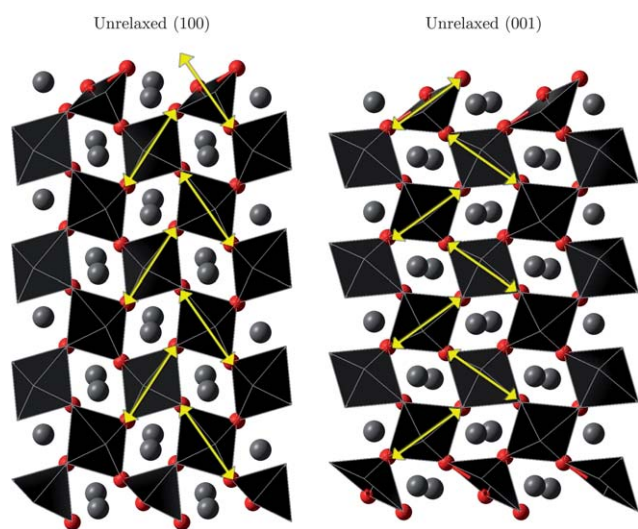## B   The Jahn–Teller effect and transition metal ion undercoordination

In order to fully explain the trend of surface formation energy for the orthorhombic AAF phase of LaMnO$_3$, it is necessary to consider not only the average Mn coordination at the surface when it is cleaved from the bulk, as described above, but also the type of Mn–O bond cleaved, the presence of under-coordinated Mn and O ions in the same octahedron and the polarisation of the undercoordinated ions. These factors were not considered in the previous works,[39,40] but are of similar importance to the number of cleaved transition metal to oxygen bonds.

The different types of bonds cleaved (apical and equatorial), the total number of Mn ions per cell in the surface layer and E_s are given in Table 4. A comparison of the (100) and (001) surfaces can be used to illustrate the difference that the type of bond cleaved makes to the surface energy. In Fig. 6 the arrows indicate the direction of the apical bonds; it is clear that the orientation of the octahedra is such that, upon cleavage of the (100) surface, a relatively weak (the longer apical) bond is cleaved. This requires less energy than cleaving the (001) surface, where a relatively strong (the shorter equatorial) bond is cleaved. Hence, the (100) surface has a lower E_s than the (001) surface, despite having the same number of cleaved Mn–O bonds overall.

The order of stability of the studied surfaces is in general agreement with the assumption that cleaving an apical Mn–O bond is more facile than cleaving an equatorial Mn–O bond. The (110) surface has the highest E_s with 1 equatorial and 2 apical bonds cleaved, and the second highest E_s corresponds to the (001) surface with 2 equatorial bonds cleaved. The remaining two surfaces both have 2 apical bonds cleaved and therefore are the lowest in energy. However, there is large discrepancy between their energies, which cannot be

Table 4 The unrelaxed surface formation energy $E_s^{Unrelaxed}$ of the stoichiometric Type 2 surfaces of orthorhombic (*Pnma*) AAF LaMnO$_3$. N_{Mn} is the number of Mn ions at the termination, $Ap^{cleaved}$ is the number of cleaved apical Mn–O bonds at the surface and $Eq^{cleaved}$ is the number of cleaved equatorial Mn–O bonds. Remaining notation is as in Table 3

Miller indices	N_{Mn}	Mn^{coord}	$Ap^{cleaved}$	$Eq^{cleaved}$	$E_s^{Unrelaxed}$ (J m^{-2})
(1 1 0)	2	4.5	2	1	2.67
(0 0 1)	2	5	0	2	2.52
(1 0 1)	4	5.5	2	0	2.25
(1 0 0)	2	5	2	0	1.47

Fig. 6 The slabs of the unrelaxed (100) and (001) surface, with arrows indicating the direction of the elongating apical (longest Mn–O bonds) J–T distortion. The shortening equatorial J–T distortion occurs perpendicular to the arrows. Remaining details are as in Fig. 2.
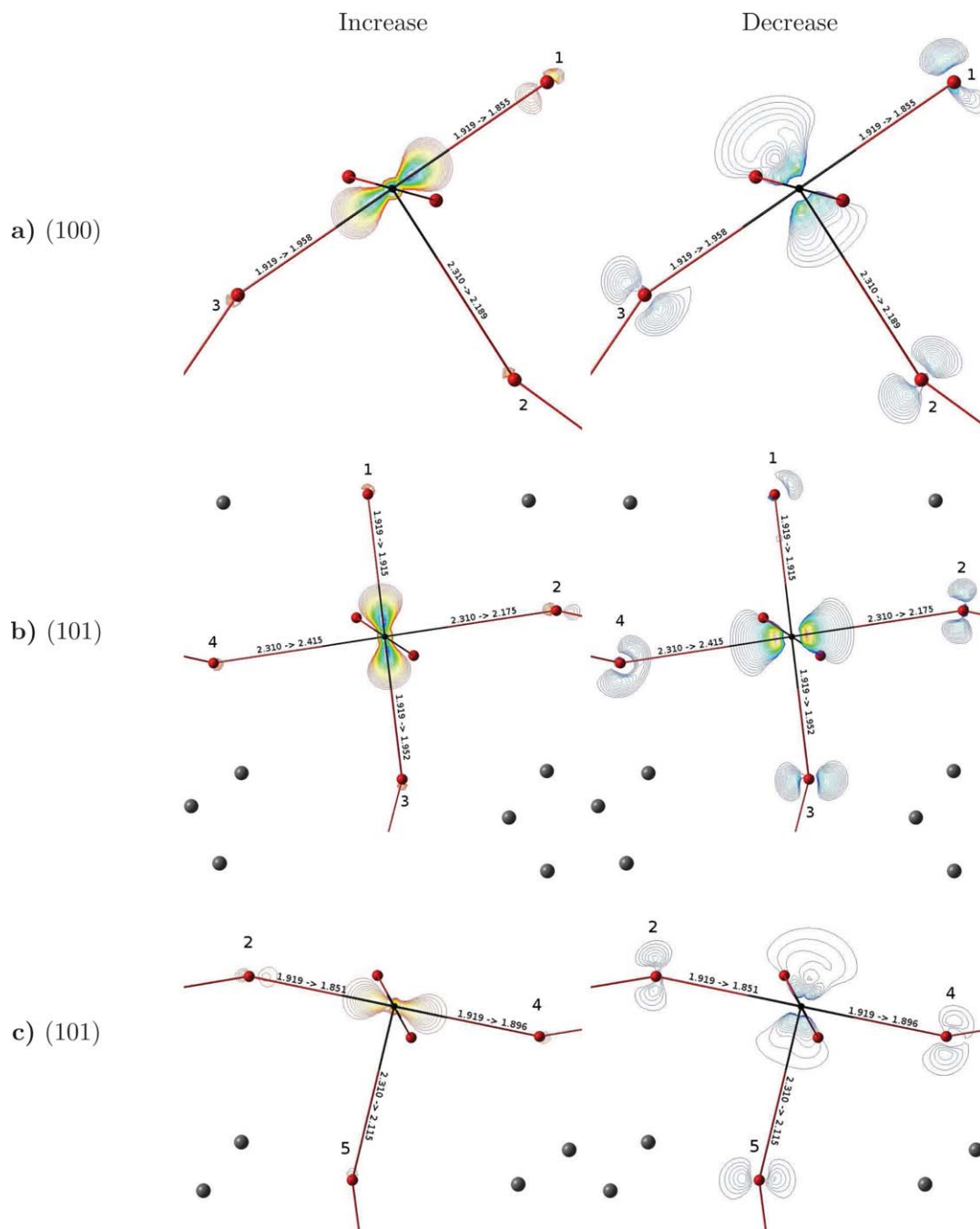
rationalised by considering only the type of Mn–O bond cleaved at the surface. The difference in energy between the (101) and (100) surfaces can be further analysed in terms of the cleavage costs of the bonds, which can be approximated by the unrelaxed surface formation energy normalised with respect to the number of bonds rather than the surface area. The (001) surface energy implies an equatorial bond cleavage energy of 5.85×10^{-19} J per bond. The energies of apical bond cleavage are 3.20×10^{-19} J per bond and 7.14×10^{-19} J per bond, when evaluated from the (100) and (101) surface energies, respectively. The (110) surface contains both apical and equatorial bonds; if we substitute the equatorial bond energy obtained from the (001) surface, the resulting apical bond cleavage energy is determined as 4.42×10^{-19} J per bond. This suggests that the energy of the apical bond cleavage for the (101) surface is exceptionally high.

The higher cost of apical bond cleavage and the corresponding higher surface formation energy of the (101) surface can be studied further by considering the differences in the local structure at the surface terminations. Upon cleaving the (101) surface (see Fig. 4), undercoordinated Mn ions and undercoordinated O ions are exposed, with each undercoordinated ion in a separate octahedron. The cleavage of the (100) surface, instead, produces an undercoordinated O and undercoordinated Mn in the same octahedron (see Fig. 5). This is the main reason for the higher bond cleavage energy of the (101) surface. A simple ionic model can be used to rationalise the differences in energy, based on the electrostatics of the cleaved octahedra. If an octahedron is cleaved so that an O ion is left monocoordinated (O ions normally coordinate to 2 Mn ions), the O ion polarises, maximising the attractive interaction with the remaining Mn ion and increasing its effective coordination. Similarly, if an octahedron is cleaved so that an Mn is 5-coordinated, the Mn ion will polarise and maximise the attractive interaction with the remaining O ions in order to increase its effective coordination. In the instance that an octahedron contains both an undercoordinated O and Mn, as in the (100) surface, then the polarisation of both ions works cooperatively so that the coordination loss of both of the ions is efficiently compensated, resulting in a lower cost of cleavage. This compensation mechanism is present in all of the surfaces, except the (101) surface where the undercoordinated ions are in separate octahedra.

C Electron density difference maps

The polarisation of the electron density on the unrelaxed surfaces due to loss of ion coordination can be explored by mapping the electron density difference with respect to a superposition of the spherical charge density of the ions (Mn^{3+}, O^{2+}), as presented in Fig. 7.† At both the (100) and (101)

† The difference maps in Fig. 7 are all generated using 50 contours. For (a) the unrelaxed 5-coordinated Mn on the (100) surface the isovalue range, measured in e/Bohr^3, is: -0.30 to -0.02 (decrease in electron density) and 0.02 to 0.21 (increase in electron density). The maps for the unrelaxed 6-coordinated Mn on the (101) surface (b) have an isovalue range of: -0.30 to -0.02 and 0.02 to 0.15. Lastly, (c) the maps for the unrelaxed 5-coordinated Mn on the (101) surface have an isovalue range of: -0.30 to -0.02 and 0.02 to 0.15.

11158 | *J. Mater. Chem. A*, 2013, **1**, 11152–11162

This journal is © The Royal Society of Chemistry 2013

Fig. 7 Difference maps (increase and decrease) between the electron density of the Mn centred octahedra at the (100) and (101) surfaces and a spherical reference density of ionic superpositions (Mn^{3+} and O^{2-}). **a)** is the unrelaxed 5-coordinated Mn on the (100) surface, with the oxygen atoms in the plane of the electron density slice labelled from 1 to 3. **b)** is the unrelaxed 6-coordinated Mn on the (101) surface, with the oxygen atoms in the plane of the electron density slice labelled 1 to 4. **c)** is the unrelaxed 5-coordinated Mn on the (101) surface, with the oxygen atoms in the plane of the electron density slice labelled 2, 4 and 5, referring to the O ions bridging the 6-coordinated Mn (2 and 4) and an additional O (5). The bond distances before – >after relaxation are given along the bonds in Å.

surfaces, it is evident that the Mn ions polarise in order to reduce the electron density in the planes of the short equatorial bonds – this decreases the strong repulsion between Mn 3d electrons and the equatorial O ions. Consequently, the Mn electron density along the longer apical bond direction increases – where the repulsion from the apical O ions is lower. This behaviour is simply a consequence of the Mn^{3+} d^4 J–T distortion and is also seen in the bulk crystal.

In addition to the polarisation due to the J–T distortion, undercoordinated surface ions polarise in order to increase their effective coordination, and thus offset some of the cost of cleavage. On the difference map of the (100) surface there are 2 notable features:

1. The electron density of the 5-coordinated Mn spreads out towards the region left vacant by the cleaved apical O ion, evident by the enlarged contours above the Mn ion and the

smaller contours in the direction of the remaining apical Mn–O bond. This reduces the repulsion between the Mn 3d electrons and the remaining apical oxygen ion (labelled as "2" in Fig. 7a), and is related to the reduction in bond length from 2.31 Å to 2.19 Å upon relaxation.

2. The electron density of the monocoordinated O along its remaining bond is reduced (see O "1" in left of Fig. 7a), which, in combination with the polarisation of the Mn ion, results in a significant decrease in repulsion between the Mn 3d electrons and the O ion. This is related to the shortening of this equatorial bond from 1.92 Å to 1.86 Å upon relaxation.

Both of these effects result in polarisation that works to increase the effective coordination of the undercoordinated ions and thus stabilising the surface. The difference maps of the (101) surface are displayed in Fig. 7b for the octahedron containing the monocoordinated O (O "1"), and Fig. 7c for its neighbouring octahedron containing the 5-coordinated Mn. The polarisation effects present on this surface are more complex than the (100) surface, because the undercoordinated ions (5-coordinated Mn and monocoordinated O) occupy separate (neighbouring) octahedra. The notable features of the maps are detailed below:

1. The polarisation of the monocoordinated O of the (101) surface is different to that in the (100) surface as it does not involve a decrease of the O electron density along the O–Mn bond (see O "1" in left of Fig. 7b). This is likely to be due to the absence of any cooperative polarisation from the 6-coordinated Mn, which does not require an increase in coordination. Since the O ion is unable to polarise to increase its effective coordination, the cleavage of the surface becomes more costly. The absence of any attractive polarisation from the monocoordinated O is evident by the relatively minor change in the O "1"-Mn bond distance upon relaxation.

2. The electron density difference around the 6-coordinated Mn on the (101) surface remains constrained and symmetric (Fig. 7b), behaving similar to that of the bulk Mn ion, while the electron density difference around its neighbouring 5-coordinated Mn (Fig. 7c) is similar to that of the 5-coordinated Mn on the (100) surface (Fig. 7a). Notably, there is a comparable reduction in the bond length between the 5-coordinated Mn and the remaining apical O, labelled as "5" in Fig. 7c (2.310 Å to 2.115 Å upon relaxation). The 5-coordinated Mn on the (101) surface is therefore also able to polarise to offset some of the cost of cleavage.

3. The strong polarisation of the 5-coordinated Mn is favourable, however, it also results in additional repulsive interactions for the neighbouring 6-coordinated Mn. The O labelled as "4" in Fig. 7b and c bridges the two Mn ions and polarises its electron density to reduce its repulsion to that of the 5-coordinated Mn. As a result, the O electron density is shifted towards the 6-coordinated Mn (note the shape of the O "4" electron density in Fig. 7b), significantly increasing the repulsion between itself and the 3d electrons of the 6-coordinated Mn. This repulsion will contribute to the higher cost of cleavage and is evident by the large increase in the length of this bond from 2.310 Å to 2.415 Å upon relaxation.

These effects further make it clear that undercoordinated ions polarise to increase their effective coordination. In particular, it evident from the (101) surface that, if a surface is cleaved so that undercoordinated counterions do not share the same octahedron, the polarisation of the ions can cause a disruptive electron repulsion that destabilises the surface and results in a higher cost of cleavage. The relaxation of such a surface will then work to restore the effective coordination of the undercoordinated ions to the bulk level.

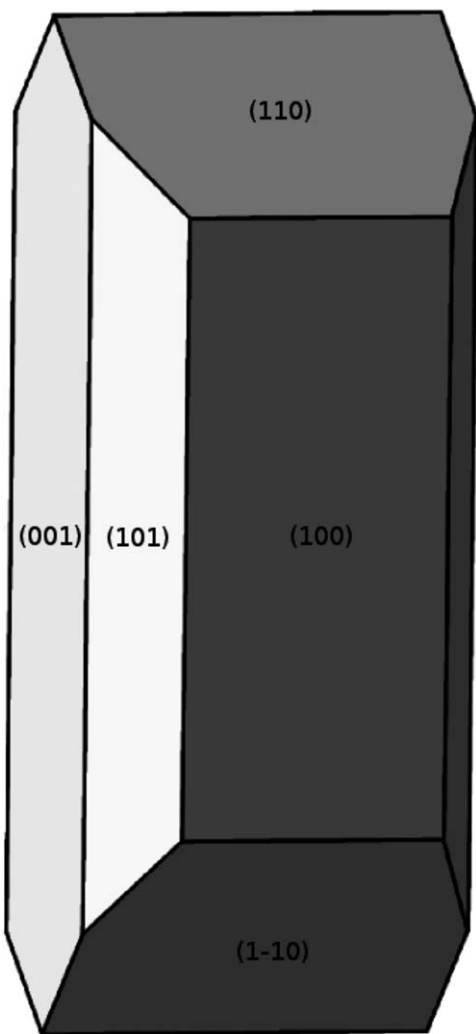To summarise, the main factors that affect the surface formation energy are:

● The strength and number of Mn–O bonds cleaved at the surface (equatorial vs. apical)

● Whether undercoordinated counterions are bound to each other to compensate for coordination loss (undercoordinated Mn and O sharing the same octahedron)

● The relaxation of the surface resulting from the polarisation of the electron density of the undercoordinated ions (aimed at restoring the effective coordination).

D Crystal shape and manganese sites

The computed surface energies have been used to predict the equilibrium crystal morphology based on a Wulff construction (see Fig. 8). It is important to highlight here that this Wulff construction is based on the restricted set of low-index surfaces and non-polar unreconstructed terminations. A crystallite in the AFC environment can potentially exhibit other surfaces, terminations and stoichiometries. Using this simplified representation we are able to study the effects of Jahn–Teller distortion, mechanisms of surface stabilisation and the nature of reaction sites in a controlled environment. This also provides the basis for systematic studies of other surfaces and terminations in the future.

The plot shows that the (100) surface is dominant, contributing 32% surface area (see Table 5). This is as expected, since the (100) surface has the lowest formation energy. The (001) and (101) surfaces also make a contribution to the area in proportion to their formation energies. It is notable that due to its orientation, the (110) surface contributes a large area (27.8%), even though it has the highest formation energy.

As part of a study on an AFC catalyst surface, it is useful to classify the various types of reaction (Mn) sites that are available on the surfaces, where the ORR can take place.[8,9] All of the surfaces studied are characterised by 5-coordinated Mn adsorption sites; 4-coordinated Mn adsorption sites also exist, but are present on only the (110) surface. In the equilibrium crystal morphology 18.6% of the Mn sites available are 4-coordinated (2/3 of the (110) sites, see Table 5), while the remainder (81.4%) are 5-coordinated. The sites are also distinguished by the changes in Mn–O bond distance due to J–T distortion and surface relaxation. If we take only the J–T distortion into consideration, we are left with four distinct Mn sites: MnO_4^{Ap}, MnO_4^{Eq}, MnO_5^{Ap} and MnO_5^{Eq}, where the labelling is based on the bond distance of the O ion cleaved to make the site. It is expected that the equatorial sites will bind adsorbates strongly while the apical sites will bind

11160 | *J. Mater. Chem. A*, 2013, **1**, 11152–11162

This journal is © The Royal Society of Chemistry 2013

Fig. 8 Wulff plot showing the equilibrium crystal morphology based on the relaxed surface formation energies.

Table 5 The Mn sites, % surface area (from the plot in Fig. 8) and formation energies E_s (in J m^{-2}) of the stoichiometric Type 2 surfaces of orthorhombic (*Pnma*) AAF LaMnO$_3$. The superscripts ^{Ap} and ^{Eq} refer to apical and equatorial bindings sites respectively (*i.e.* the type of O ion cleaved to form the site)

Miller indices	$E_s^{Relaxed}$	Surface area (%)	Mn sites
(1 1 0)	1.98	27.8	1 MnO$_5^{Ap}$ & 1 MnO$_4^{Ap+Eq}$
(0 0 1)	1.39	19.9	2 MnO$_5^{Eq}$
(1 0 1)	1.36	20.1	2 MnO$_5^{Ap}$
(1 0 0)	0.98	32.3	2 MnO$_5^{Ap}$

adsorbates weakly. The types of site available on each surface are presented in Table 5, and the total contribution of each site is: MnO$_5^{Ap}$ – 61.7%, MnO$_5^{Eq}$ – 19.9%, MnO$_4^{Ap}$ – 9.3%, MnO$_4^{Eq}$ – 9.3%.

The activity of a reaction is likely to be critically dependant on the strength with which a reactant adsorbs on a catalyst site, where a balance between strong and weak adsorption is sought. This has been shown to be the case for the ORR reaction on a range of perovskites where the binding strength between the transition metal site and O$_2$ has been found to be near optimal on a LaMnO$_3$ powder sample prepared *via* a co-precipitation method.[9] In this study, however, the range of adsorption sites available on the LaMnO$_3$ powder and the differences in binding strength that J–T distortion could introduce were not considered. Based on the current work it is likely that a further distinction related to the type of site is possible. The investigation of these adsorption sites is key to the optimisation of ORR catalysis in AFCs. Once the best adsorption sites have been identified, using our understanding of the surface thermodynamics it may be possible to tailor the LaMnO$_3$ crystal morphology and increase the proportion of sites which are more active.[10,39]

V   Conclusions

In this work we have presented a detailed investigation into the structure and energetics of the unreconstructed stoichiometric surfaces of orthorhombic AAF LaMnO$_3$ using hybrid-exchange density functional theory. We have determined the order of stability for the surfaces to be (low energy) (100) < (101) < (001) < (110) (high energy). The calculated equilibrium crystal morphology indicates that the surface area contribution of the (100) surface is dominant (32.3%), followed by the contribution of the (110) surface (27.8%). The most widely available adsorption site for the oxygen reduction reaction is an apically cleaved MnO$_5$ octahedra, making up to 61.7% of the Mn sites. The second most widely available site is an equatorially cleaved MnO$_5$ octahedra, at 19.9% of the Mn sites.

Analysis of the surface terminations with respect to the surface formation energies has revealed that the Mn coordination is insufficient to explain the relative stability of the surfaces, contrary to previous work.[39,40] It is also necessary to consider; (1) the strength and number of cleaved Mn–O bonds, (2) the compensation of undercoordinated ions at the terminations and (3) the relaxation from the bulk geometry.

These factors form the basis for rationalising the surface formation energy in transition metal oxides. Equally, the crystal morphology and predicted adsorption sites provide the groundwork for analysing the catalytic activity of LaMnO$_3$.

Acknowledgements

References

1 S. Jin, T. H. Tiefel, M. McCormack, R. A. Fastnacht, R. Ramesh and L. H. Chen, *Science*, 1994, **264**, 413–415.

2 S. Tao, J. Irvine and J. Kilner, *Adv. Mater.*, 2005, **17**, 1734–1737.

3 T. Ishihara, *Perovskite Oxide for Solid Oxide Fuel Cells*, Springer, 2009.

4 D. T. Morelli, A. M. Mance, J. V. Mantese and A. L. Micheli, *J. Appl. Phys.*, 1996, **79**, 373–375.

5 M. Yuasa, M. Nishida, T. Kida, N. Yamazoe and K. Shimanoe, *J. Electrochem. Soc.*, 2011, **158**, A605–A610.

6 M. Hayashi, H. Uemura, K. Shimanoe, N. Miura and N. Yamazoe, *J. Electrochem. Soc.*, 2004, **151**, A158–A163.

7 D. B. Meadowcroft, *Nature*, 1970, **226**, 847–848.

8 F. Bidault, D. Brett, P. Middleton and N. Brandon, *J. Power Sources*, 2009, **187**, 39–48.

9 J. Suntivich, H. A. Gasteiger, N. Yabuuchi, H. Nakanishi, J. B. Goodenough and Y. Shao-Horn, *Nat. Chem.*, 2011, **3**, 546–550.

10 E. A. Ahmad, L. Liborio, D. Kramer, G. Mallia, A. R. Kucernak and N. M. Harrison, *Phys. Rev. B: Condens. Matter Mater. Phys.*, 2011, **84**, 085137.

11 E. O. Wollan and W. C. Koehler, *Phys. Rev.*, 1955, **100**, 545–563.

12 J. Rodríguez-Carvajal, M. Hennion, F. Moussa, A. H. Moudden, L. Pinsard and A. Revcolevschi, *Phys. Rev. B: Condens. Matter Mater. Phys.*, 1998, **57**, R3189–R3192.

13 R. A. Evarestov, E. A. Kotomin, D. Fuks, J. Felsteiner and J. Maier, *Appl. Surf. Sci.*, 2004, **238**, 457–463.

14 S. Piskunov, E. Heifets, T. Jacob, E. A. Kotomin, D. E. Ellis and E. Spohr, *Phys. Rev. B: Condens. Matter Mater. Phys.*, 2008, **78**, 121406.

15 Y. Mastrikov, E. Heifets, E. Kotomin and J. Maier, *Surf. Sci.*, 2009, **603**, 326–335.

16 E. A. Kotomin, Y. Mastrikov, E. Heifets and J. Maier, *Phys. Chem. Chem. Phys.*, 2008, **10**, 4644–4649.

17 Y. Choi, D. S. Mebane, M. C. Lin and M. Liu, *Chem. Mater.*, 2007, **19**, 1690–1699.

18 Y. Choi, M. E. Lynch, M. C. Lin and M. Liu, *J. Phys. Chem. C*, 2009, **113**, 7290–7297.

19 Y. Wang and H.-P. Cheng, *J. Phys. Chem. C*, 2013, **117**, 2106–2112.

20 D. Muñoz, N. M. Harrison and F. Illas, *Phys. Rev. B: Condens. Matter Mater. Phys.*, 2004, **69**, 085115.

21 J. B. Goodenough and J.-S. Zhou, *J. Mater. Chem.*, 2007, **17**, 2394–2405.

22 F. Tang, M. Huang, W. Lu and W. Yu, *Surf. Sci.*, 2009, **603**, 949–954.

23 A. D. Becke, *J. Chem. Phys.*, 1993, **98**, 5648.

24 R. Dovesi, V. R. Saunders, C. Roetti, R. Orlando, C. M. Zicovich-Wilson, F. Pascale, B. Civalleri, K. Doll, N. Harrison, I. Bush, P. D'Arco and M. Llunell, CRYSTAL09 *User's Manual*, Università di Torino, Torino, 2010.

25 J. Muscat, A. Wander and N. Harrison, *Chem. Phys. Lett.*, 2001, **342**, 397–401.

26 G. Mallia and N. M. Harrison, *Phys. Rev. B: Condens. Matter Mater. Phys.*, 2007, **75**, 165201.

27 N. C. Wilson, S. P. Russo, J. Muscat and N. M. Harrison, *Phys. Rev. B: Condens. Matter Mater. Phys.*, 2005, **72**, 024110.

28 F. Cora, M. Alfredsson, G. Mallia, D. S. Middlemiss, W. C. Mackrodt, R. Dovesi and R. Orlando, *The Performance of Hybrid Density Functionals in Solid State Chemistry*, Springer Berlin/Heidelberg, 2004, vol. 113, pp. 171–232.

29 G. C. De Fusco, B. Montanari and N. M. Harrison, *Phys. Rev. B: Condens. Matter Mater. Phys.*, 2010, **82**, 220404.

30 L. Ge, J. H. Jefferson, B. Montanari, N. M. Harrison, D. G. Pettifor and G. A. D. Briggs, *ACS Nano*, 2009, **3**, 1069–1076.

31 G. C. De Fusco, L. Pisani, B. Montanari and N. M. Harrison, *Phys. Rev. B: Condens. Matter Mater. Phys.*, 2009, **79**, 085201.

32 L. Liborio, G. Mallia and N. Harrison, *Phys. Rev. B: Condens. Matter Mater. Phys.*, 2009, **79**, 245133.

33 C. L. Bailey, L. Liborio, G. Mallia, S. Tomić and N. M. Harrison, *Phys. Rev. B: Condens. Matter Mater. Phys.*, 2010, **81**, 205214.

34 L. M. Liborio, C. L. Bailey, G. Mallia, S. Tomic and N. M. Harrison, *J. Appl. Phys.*, 2011, **109**, 023519.

35 P. W. Tasker, *J. Phys. C: Solid State Phys.*, 1979, **12**, 4977.

36 http://www.crystal.unito.it/Basis_Sets/Ptable.html.

37 G. Mallia, R. Orlando, M. Llunell and R. Dovesi, *Computational Materials Science*, IOS Press, Amsterdam, 2003, vol. 187, pp. 102–121.

38 C. Pisani, R. Dovesi and C. Roetti, *Hartree-Fock ab initio Treatment of Crystalline Systems*, Springer Verlag, Heidelberg, 1988, vol. 48.

39 D. Kramer and G. Ceder, *Chem. Mater.*, 2009, **21**, 3799–3809.

40 L. Wang, F. Zhou, Y. S. Meng and G. Ceder, *Phys. Rev. B: Condens. Matter Mater. Phys.*, 2007, **76**, 165435.

41 http://cci.lbl.gov/.

42 http://www.cryst.ehu.es/.

43 M. J. Akhtar, C. R. A. Catlow, B. Slater, A. M. Walker and S. M. Woodley, *Chem. Mater.*, 2006, **18**, 1552–1560.

44 R. A. Evarestov, E. A. Kotomin, Y. A. Mastrikov, D. Gryaznov, E. Heifets and J. Maier, *Phys. Rev. B: Condens. Matter Mater. Phys.*, 2005, **72**, 214411.